Article

Scratch-Induced Wear Behavior of Multi-Component Ultra-High-Temperature Ceramics

Gia Garino [†], Ambreen Nisar *,[†] , Abhijith K. Sukumaran and Arvind Agarwal

Plasma Forming Laboratory, Department of Mechanical and Materials Engineering, Florida International University, Miami, FL 33174, USA; ggari005@fiu.edu (G.G.); asuku002@fiu.edu (A.K.S.); agarwala@fiu.edu (A.A.)
* Correspondence: anisar@fiu.edu
[†] These authors contributed equally to this work.

Abstract: Multi-component ultra-high-temperature ceramics (MC-UHTCs) are promising for high-temperature applications due to exceptional thermo-mechanical properties, yet their wear characteristics remain unexplored. Herein, the wear behavior of binary (Ta, Nb)C, ternary (Ta, Nb, Hf)C, and quaternary (Ta, Nb, Hf, Ti)C UHTCs synthesized via spark plasma sintering (SPS) is investigated. Gradual addition of equimolar UHTC components improves the wear resistance of MC-UHTCs, respectively, by ~29% in ternary UHTCs and ~49% in quaternary UHTCs when compared to binary UHTCs. Similarly, the penetration depth decreased from 115.14 mm in binary UHTCs to 73.48 mm in ternary UHTCs and 44.41 mm in quaternary UHTCs. This has been attributed to the complete solid solutioning, near-full densification and higher hardness (~up to 30%) in quaternary UHTCs. Analysis of the worn-out surface suggests pull-out, radial, and edge micro-cracking and delamination as the dominant wear mechanisms in binary and ternary UHTCs. However, grain deformation and minor delamination are the dominant wear mechanisms in quaternary UHTCs. This study underscores the potential of MC-UHTCs for tribological applications where material experiences removal and inelastic deformation under high mechanical loading.

Keywords: multi-component ultra-high-temperature ceramics (MC-UHTCs); solid solution; spark plasma sintering (SPS); wear resistance; penetration depth

1. Introduction

Ultra-high-temperature ceramics (UHTCs) have gained significant attention due to their excellent mechanical properties, oxidation resistance, and melting temperatures > 3000 °C [1]. UHTCs are classified as borides, carbides, and nitrides of transition metal elements from groups IV and V [1,2]. Among them, transition metal carbides such as TaC, NbC, HfC, ZrC, and TiC are widely utilized UHTC carbides known for their outstanding thermo-mechanical properties. The literature on UHTCs and their possible application in nuclear reactors, hypersonic vehicles, and rockets' nose cones to support melting conditions has been studied for decades [1–4]. However, none of the unary UHTC components have been able to accommodate all the demanding requirements of extreme environments. To counter this, one approach is the reinforcement of the second phase, such as Si and carbon-based additives (carbon nanotubes, graphene), in UHTCs to enhance oxidation resistance and fracture toughness [5–8].

Another approach is adapted from the recent development by applying the concept of high-entropy alloys (HEA) to a wide range of ceramics [9–11] such as oxides [12], borides [13–15], carbides [13,14,16], and nitrides [10,17,18]. By employing HEA concepts in UHTCs, high-entropy UHTCs (HE-UHTCs) are obtained by adding equimolar compositions of four or more UHTCs. Because of their mutual solubility [11,19], these materials tend to favor the formation of complete solid-solution single phases. Their mutual solubility does not necessitate the entropy to be "high entropy"; hence, authors are in favor

of referring to HE-UHTCs as multi-component UHTCs (MC-UHTCs) [11]. Even though the entropy remains medium, these materials are characterized by a higher degree of disorder in the atomic level, leading to unique material properties such as high mechanical strength, thermal stability, and resistance to oxidation even at extreme temperatures [11]. MC-UHTCs have garnered significant interest as appealing materials for thermal protection systems (TPSs) in structural components, such as hot structures and pointed leading edges found in re-entry vehicles. These materials have attracted rapid attention due to their impressive attributes, which encompass enhanced mechanical characteristics [6,20], increased fracture toughness [21,22], resistance to creep [23], and low thermal conductivity [24,25]. However, to date, there are only a few studies investigating the wear behavior of MC-UHTCs [26–29].

Predicting the safe service life of engineering components requires accounting for wear from dynamic loads caused by atmospheric debris. Micro-particles in the atmosphere can cause plastic deformation of UHTCs [30]. Therefore, studying the abrasion resistance and damage behavior of MC-UHTCS is essential. The micro-scratch test has been widely recognized as a reliable alternative to conventional wear tests, especially for hard ceramics [31–33]. Sun et al. [26] achieved a uniform composition in (Hf–Mo–Nb–Ta–Ti) C ceramics via SPS, reporting outstanding wear resistance due to a synergistic effect of tribo-film formation and enhanced mechanical properties. Dusza et al. [29] developed (Hf–Zr–Ta–Nb–Ti) C high-entropy carbide with high density. These materials displayed high hardness and good tribological properties, primarily attributed to mechanical wear with limited grain pullout and localized tribolayer formation.

Recently, authors have reported the processing, mechanical, and oxidation behavior of binary (Ta, Nb)C, ternary (Ta, Nb, Hf)C, and quaternary (Ta, Nb, Hf, Ti)C UHTCs processed via SPS [34–36]; therefore, it is imperative to look into the wear behavior of these materials. This study reveals that MC-UHTCs (ternary and quaternary) have remarkable thermo-mechanical properties compared to unary and binary UHTC. The results showed that the mechanical properties improved considerably up to 72% for quaternary UHTCs. Moreover, the oxidation rate for binary UHTCs was 0.97 mm/s, while it was negligible in MC-UHTCs, attributed to mixed complex oxide-phase formation with $Hf_6Ta_2O_{17}$ as a major phase in the MC-UHTC system [34,35]. Herein, scratch-induced tribological characteristics and wear mechanisms of these materials are investigated. An effort is made to establish a correlation between the microstructure and mechanical and wear properties with the gradual addition of UHTC components in MC-UHTCs.

2. Materials and Methods

2.1. Solid-Solution Synthesis of MC-UHTCs

The starting materials employed in this study included commercially available UHTC powders. These powders consisted of a binary system; (Ta, Nb)C (a pre-allowed powder of 20 wt.% NbC, 80 wt.% TaC with a particle size of ~0.80 μm: Inframat Advanced Materials, LLC, Manchester, CT, USA) was procured. Additionally, unary UHTC powders of HfC (>99.5% purity, particle size ~0.33 μm; Materion LLC, Cleveland, OH, USA) and TiC (>99.9% purity, particle size < 3 μm, Inframat Advanced Materials, LLC) were procured. For ternary and quaternary UHTC systems, an equimolar concentration of each powder was utilized. The powder mixtures were ball-milled (Across International LLC, Livingston, NJ, USA) in a WC jar using WC balls (6 mm diameter) with a ball-to-powder weight ratio of 1:3 for 60 min. Further, the composite powders were consolidated using the spark plasma sintering (SPS, Model 104; Thermal Technologies, Santa Rosa, CA, USA) process with a heating rate of 100 °C/min at 1850 °C and 60 MPa for 10 min. Post sintering, a single solid-solution phase was achieved, with a relative densification of ~86% for binary UHTC and ~100% for ternary and quaternary UHTCs. Information regarding the initial powders, ball-milled powders, sintering processes, and their thermo-mechanical properties can be referenced in the authors' recent publications [34–36].

2.2. Scratch Testing and Characterization of Worn Surface

SPS pellets were sectioned using a high-speed saw (Techcut 5X precision, Allied High-Tech Products, Inc., Compton, CA, USA). After mounting, the samples underwent a grinding process using diamond grit until a surface roughness of up to 6 μm was achieved. Subsequently, cloth polishing was employed with alumina suspension to attain a surface finish of ≤1 μm. The scratch tests were performed using a micro-scratch tester (Revtest scratch tester RST[3], Anton Paar, Inc. Houston, TX, USA) with a Rockwell indenter (tip radius: 50 mm) under progressive load conditions. The load varied from 1 N to 50 N with a speed of 2 mm/min and a scratch length of 3 mm. During the test, data on acoustic emission (AE), coefficient of friction (CoF), penetration depth, and residual depths were recorded. Moreover, it generates a panoramic image of the scratch using its integrated optical microscope. Three scratches were made on each sample and the scratch paths were analyzed using FESEM (FESEM, JEOL-F100 FESEM JEOL Ltd., Akishima, Tokyo, Japan) to gain insights into the positions of cracks, delamination, and the various types of deformation that occurred on the samples during the scratching process. Optical profilometry (Nanovea, Irvine, CA, USA) was utilized to assess the surface roughness and wear track profile of the tested samples. To calculate the wear volume of the scratches, the top-view scratch image obtained from optical profilometry was analyzed using Mountains Lab Premium 10 software (Digital Surf, Besancon, France).

3. Results and Discussion

3.1. Microstructural Analysis of MC-UHTCs

The typical fractured microstructure and corresponding elemental composition of the investigated MC-UHTC samples are illustrated in Figure 1 via EDS spectra. The porosity observed in the microstructure aligns well with the densification values, being ~86% for binary (Figure 1a; Table 1) and ~100% for ternary and quaternary UHTCs (Figure 1b,c; Table 1). Consistent with the previous finding [34], segregation of HfC particles is evident in the fractured micrograph of ternary UHTCs (Figure 1b). It is important to mention here that binary and ternary UHTCs have segregation of secondary phases of NbC and HfC, while the quaternary UHTC showed complete single solid-solution phase formation, revealed from the high-resolution microscopy [36]. The presence of closely spaced intense slip lines is evident in ternary and quaternary UHTCs. These slip lines in UHTCs and MC-UHTCs are associated with a material's ability to resist deformation under higher loading conditions [37].

Table 1. Relative densification, elastic modulus, hardness, CoF, and maximum penetration depth of binary, ternary and quaternary UHTCs.

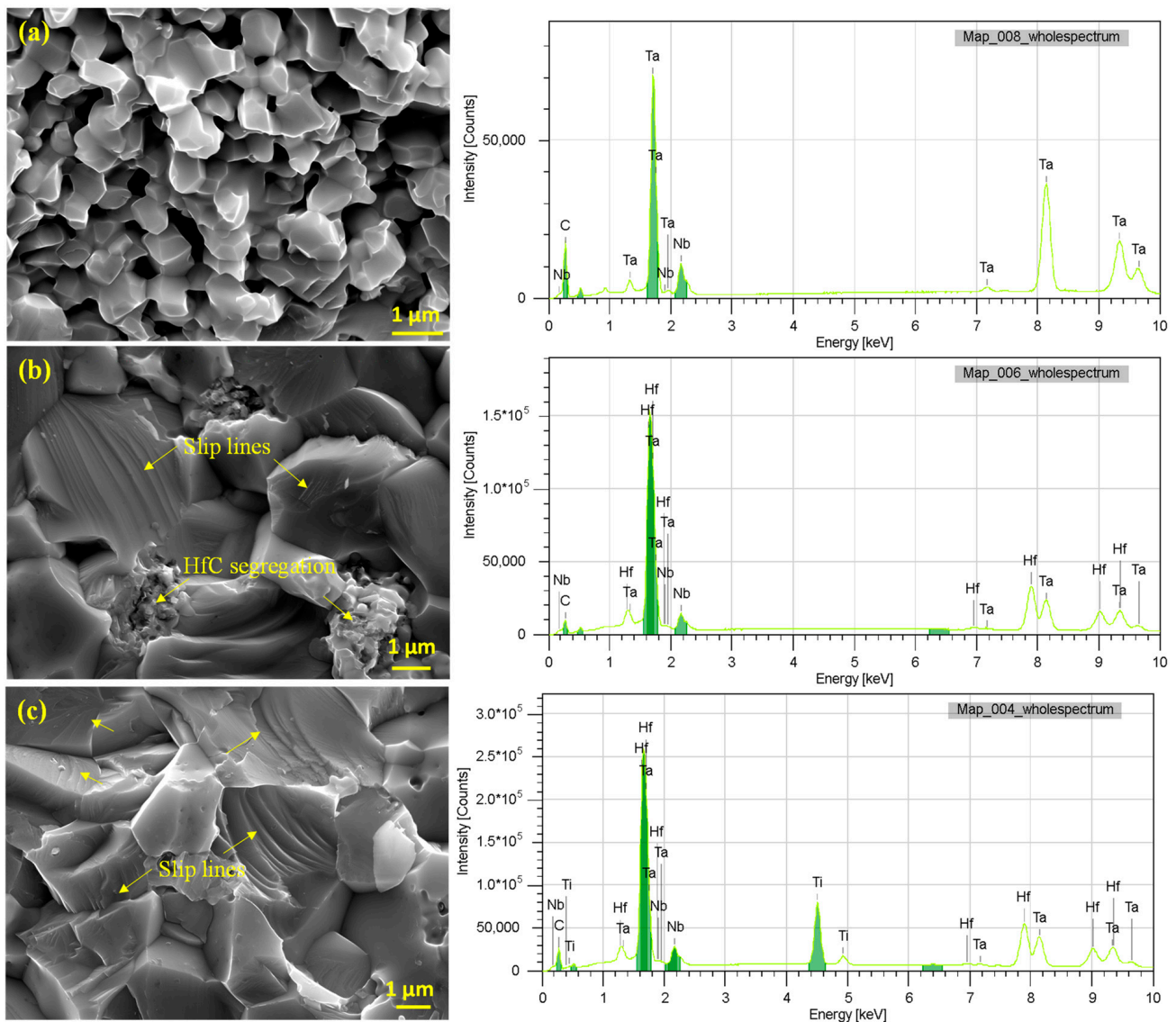| Samples	Densification (%) [34]	Elastic modulus, E (GPa) [34]	Hardness, H (GPa) [34]	CoF	Max. Penetration Depth (μm)
Binary	84	307.52 ± 36.07	15.23 ± 4.51	0.741–0.198	115.14 ± 5.23
Ternary	100	403.66 ± 9.93	33.67 ± 1.69	0.635–0.155	73.48 ± 6.02
Quaternary	100	381.16 ± 9.82	34.82 ± 2.27	0.615–0.113	44.41 ± 4.82

Figure 1. Fractured micrographs and corresponding EDS spectra showing the elemental composition of (**a**) binary, (**b**) ternary, and (**c**) quaternary UHTCs.

3.2. Wear Behavior of MC-UHTCs

The scratch-induced wear behavior test under progressive loading from 1 N to 50 N was conducted on the polished surfaces of binary, ternary and quaternary UHTCs. Figure 2 shows the variation in the coefficient of friction (CoF) and penetration depth with scratch distance in MC-UHTCs. Both CoF and penetration depth were found to increase with the progressive loading in all the samples. Table 1 shows the comparative densification, mechanical properties and wear parameters of binary, ternary and quaternary UHTCs. Based on the three tests carried out on these samples, the average CoFs (Figure 2a, Table 1) for binary, ternary and quaternary UHTCs are 0.43, 0.41, and 0.34, respectively. Similarly, the penetration depth decreased from ~115.14 mm in binary to 73.48 mm in ternary and 44.41 mm in quaternary UHTCs. The decreasing trend in CoF as well as the penetration depth has been attributed to the reduction in deformation under the applied load elicited from the higher densification and hardness in quaternary UHTCs (see Table 1) [34].
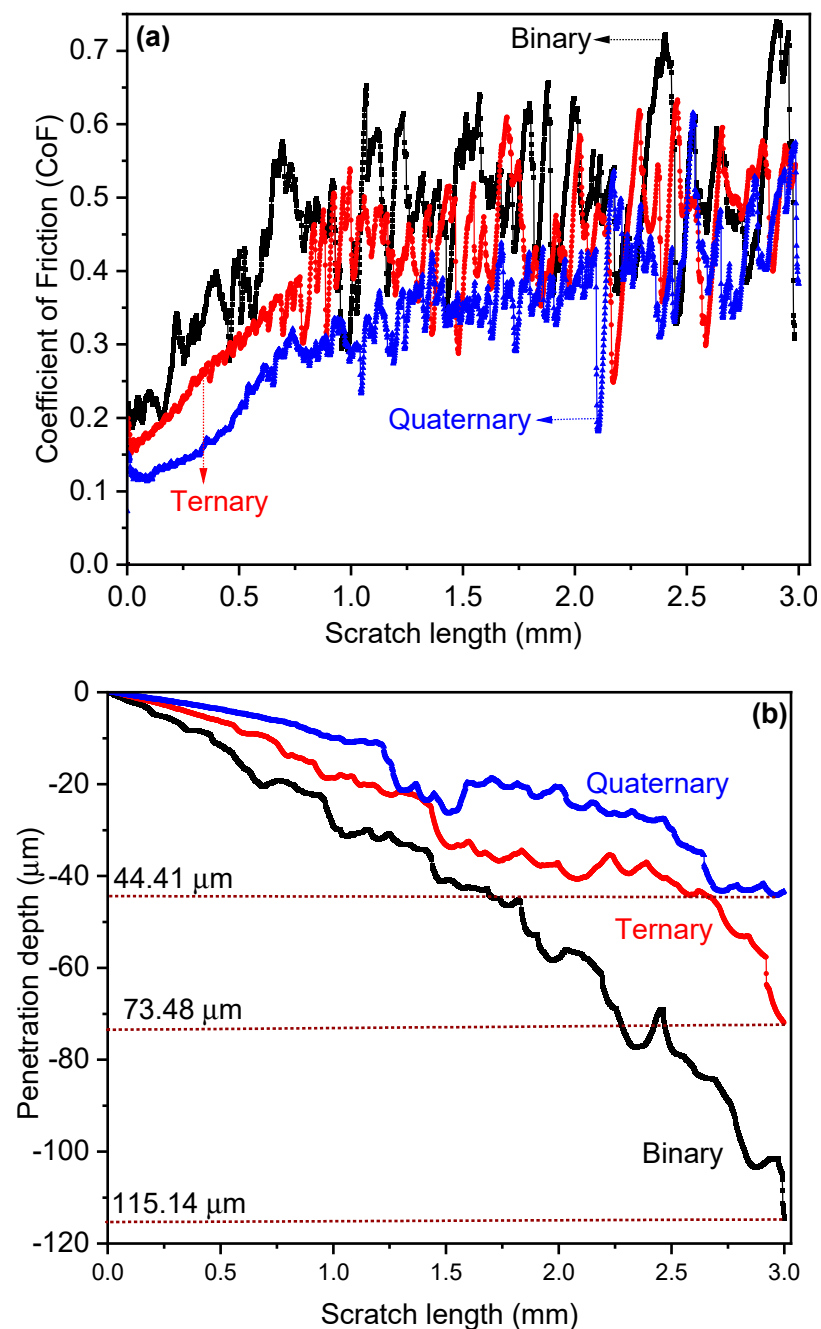
Figure 2. (**a**) Coefficient of friction (CoF) and (**b**) penetration depth of binary, ternary and quaternary UHTCs measured during progressive scratch testing (load variation: 1 N to 50 N; scratch length: 3 mm).

The typical aspect of the scratch-induced deformation is revealed from the superimposed SEM image, optical profilometry and acoustic emission (AE) data of 3 mm scratching in MC-UHTCs, shown in Figure 3. It is to be noted here that the overall scratch track shows deeper grooves in binary UHTCs followed by ternary and quaternary UHTCs, as seen from the SEM images in Figure 3. The perturbations in the AE plot, similar to the CoF and penetration depth plots, are attributed to the interaction of the tip with the porosity, pile-ups and with scratch-induced deformation in the material. Based on the depths seen in the optical profilometry (color-coded as light-green, turquoise, blue and darker blue regions), four critical loads at which events such as cracking, chipping, propagation and fracture occur in the samples are compared in Table 2. The load at which cracking initiates

(Fc$_1$) increased from 6.9 N (in binary) to 10.4 N (in ternary) and 18.5 N (in quaternary). Similarly, the loads at which cracking propagates (Fc$_2$) increased from 17.6 N (in binary) to 25.3 N (in ternary) and 37.9 N (in quaternary). Finally, the fracture (Fc$_3$) begins at 28.6 N in binary UHTCs, 43.6 N in ternary UHTCs and 48.1 N in quaternary UHTCs. It is to be noted that binary and ternary samples showed more fracture (Fc$_4$) along the progressive scratch length, respectively, at 46.5 N and 47.3 N based on the mapped optical profilometry and AE plot. The typical scratch width at the maximum loading (50 N) decreased from 354.07 mm in binary UHTCs to 245.78 µm in ternary and 207.12 µm in quaternary UHTCs. The result also suggests a high load-bearing ability of quaternary UHTCs compared to binary and ternary UHTCs. This has been attributed to near-full densification, processing-induced complete solid solutioning, and defects such as dislocations, inter-grain twisting and plasticity [36], revealed from high resolution microscopy in quaternary UHTCs. The wear volume arising from the overall scratch track (see Figure 3), presented in Table 2, backs up these findings. The quaternary UHTC, (Ta, Nb, Hf, Ti)C, has least wear volume loss of 3.16×10^{-3} mm^3 calculated for a scratch length of 3 mm and progressive loading ranging from 1 to 50 N. It is to be mentioned here that the wear volume loss for the (HfMoTiWZr)C sample against an Al$_2$O$_3$ ball with a sliding speed of 6 mm/s, sliding distance of 200 m and wear track length of 2 mm is ~2.1×10^{-4} mm^3 [27]. Compared to the binary UHTC, an improvement in the wear resistance, respectively, by 29% and 49% is observed for ternary and quaternary UHTCs. The improved wear resistance resonates well with the CoF, penetration depth and hardness values. This shows that the addition of components in MC-UHTCs does increase the wear resistance of the material.

Table 2. Values of critical loads, scratch width and wear volume during the progressive load testing of binary, ternary and quaternary UHTCs.

Samples	Critical Loads (N)				Scratch Width at Max. Load (mm)	Wear Volume ($\times 10^{-3}$ mm^3)
	Fc$_1$	Fc$_2$	Fc$_3$	Fc$_4$		
Binary	6.9	17.6	28.6	46.5	354.07 ± 53.11	6.18 ± 0.91
Ternary	10.4	25.3	43.6	47.3	245.78 ± 62.54	4.38 ± 0.87
Quaternary	18.5	37.9	48.1	N.A.	207.12 ± 28.68	3.16 ± 0.03

Further, the SEM images shown in Figure 4 reveal the damage and failure mechanism in the binary UHTC. Based on the AE data, SEM images at the most critical regions corresponding to binary samples are compared in Figure 4. It is clear from Figure 4b that even under a lower loading condition in the binary sample, debris and grain deformation are seen. As the load progresses, the severe crack networking (Figure 4c,e), fracture grains and delamination are noted (Figure 4d,e). Moreover, critical damage is attributed to the edge and radial cracking observed in Figure 4c,e. This is due to the progressive increase in tangential stress. Heightened localized stress concentration induces a decrease in the systems' energy by instigating the formation and propagation ion of micro-cracks and radial cracks.

Similarly, the damage and failure mechanism in the ternary UHTC can be understood from the SEM micrographs shown in Figure 5. Under lower loading conditions in the ternary UHTC, grain pull-out/deformation and lateral micro-cracking along with unaffected regions are seen in Figure 5b (marked region in Figure 5a). As the load progresses, the cracking at the scratch edge progresses (marked in Figure 5a) along with grain deformation, as well as some fracture and delamination (Figure 5c,d). It is important to highlight that at higher loads, evidence of unaffected areas is seen (Figure 5c,d), in contrast to the binary UHTC. This remarks the improvement in wear resistance from binary to ternary UHTCs. The presence of slip lines near the fractured region in Figure 5e elicits the superior resistance against applied load during scratch testing when compared with the binary UHTC. Such microscopic slip lines indicate the occurrence of dislocation-induced plastic deformation and dislocation mobility at room temperature [37]. This has also been

evidenced by the high load indentation and flexural strength behavior of ternary UHTCs reported elsewhere [34,36].
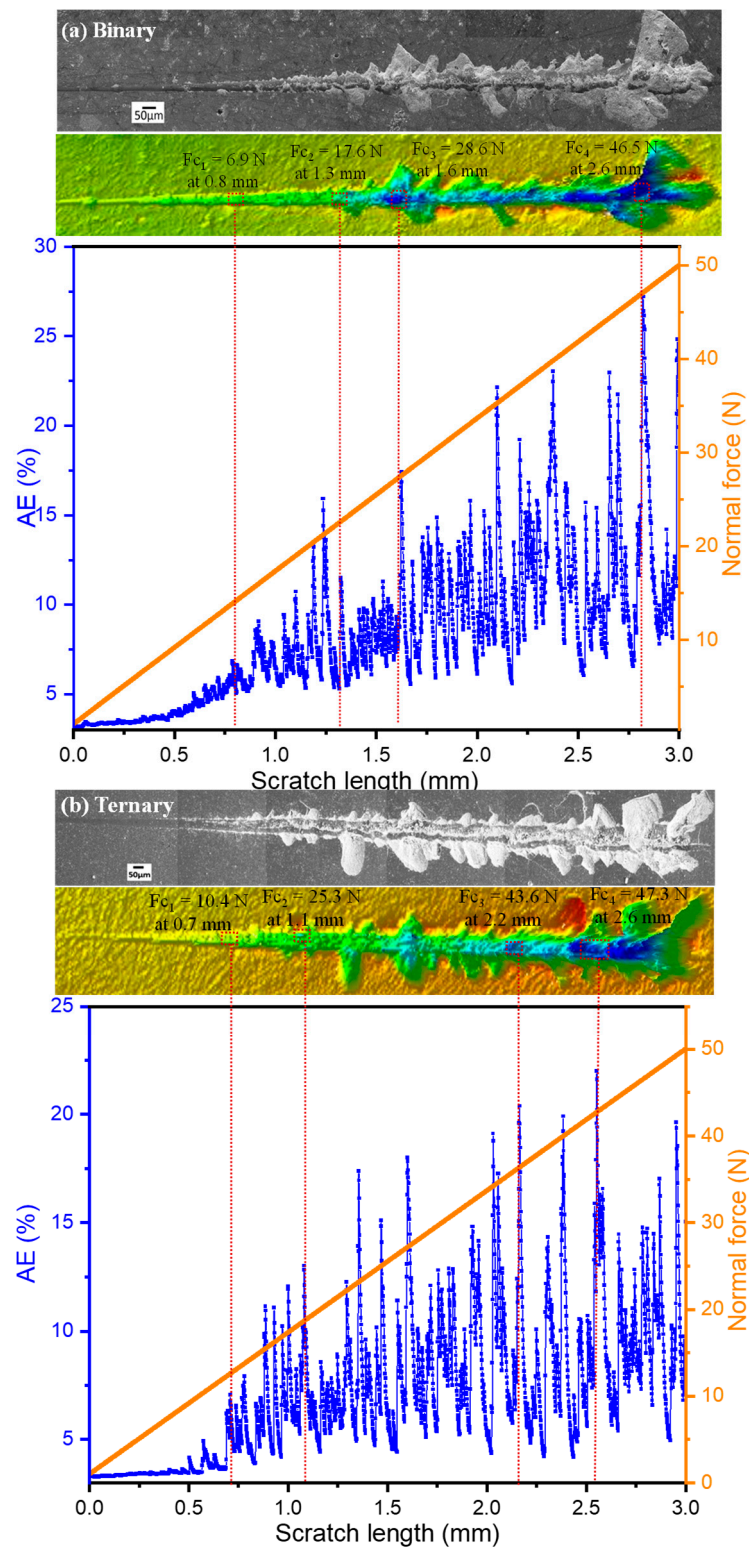

Figure 3. *Cont.*
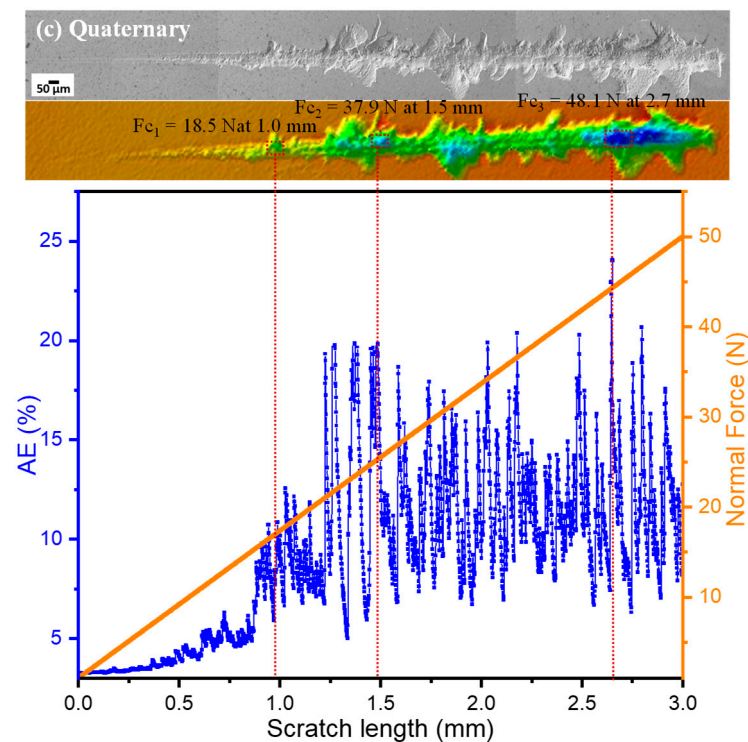
Figure 3. Superimposed SEM, profilometry images and AE data obtained during the scratch testing of (**a**) binary, (**b**) ternary, and (**c**) quaternary UHTCs.
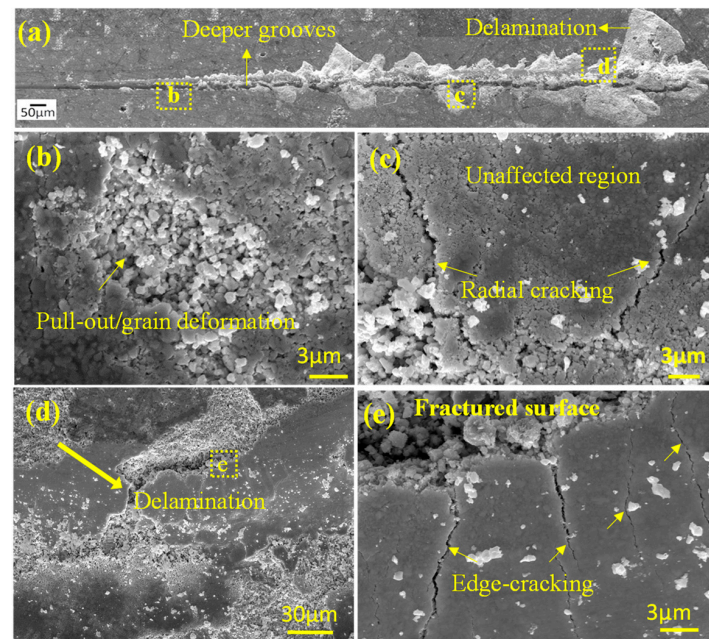

Figure 4. SEM micrographs of the (**a**) 3 mm progressive scratch track and (**b**–**e**) high magnification of the selected regions eliciting wear behavior in binary UHTCs.

Lastly, the SEM images eliciting the deformation in the quaternary UHTC during progressive scratch testing are presented in Figure 6. At lower load, most of the regions are unaffected (by the indenter during scratch loading) along with minor pull-out grain deformation; see Figure 6b. Comparing all the samples microstructurally, the presence of unaffected regions is most notable in the quaternary UHTC. As the load progressively increases in Figure 6c, grain deformation and pull-out increase. Even at the higher loading,

no micro-cracking was noticed, while most of the regions in the sample are unaffected (marked as dotted island area). This shows the improved wear resistance of the quaternary sample, attributed to its high hardness of 44.82 GPa (see Table 1). Under maximum loading conditions, some minor delamination, cracking, and pull-out are evident in Figure 6d. In quaternary UHTCs, the presence of multiple closely spaced slip lines (Figure 6e) is evident at several places throughout the progressive loading. This further confirms the ability of quaternary UHTCs to undergo plastic deformation, improving their wear resistance over binary and ternary UHTCs. In summary, pull-out, radial, and edge micro-cracking and delamination are the dominant wear mechanisms in binary and ternary UHTCs. However, in a quaternary system, grain deformation and minor delamination are the dominant wear mechanisms.
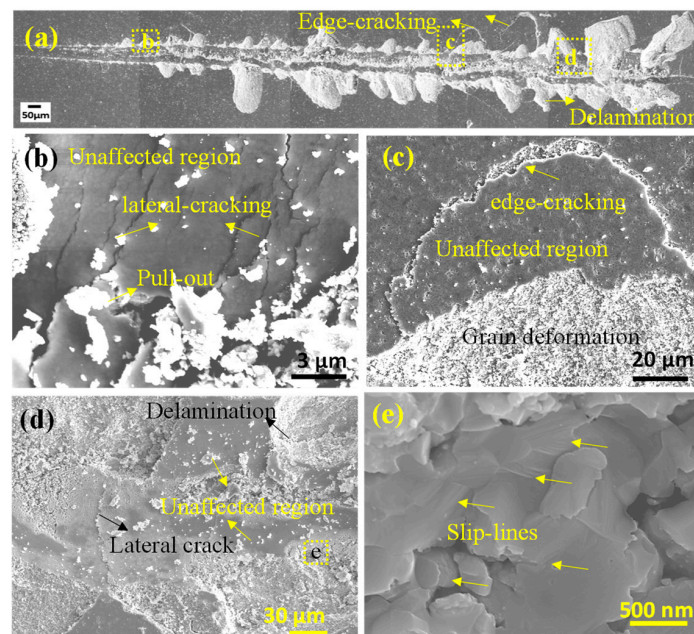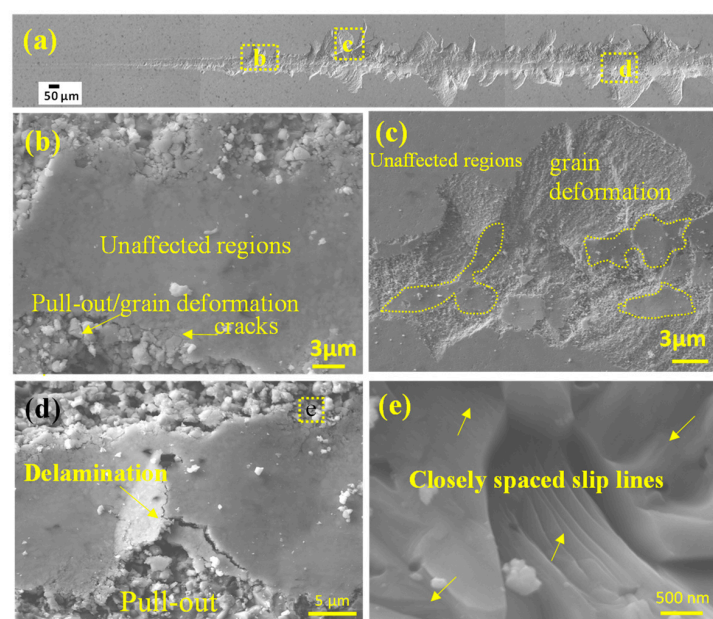

Figure 5. SEM micrographs of the (**a**) 3 mm progressive scratch track and (**b**–**e**) high magnification of the selected regions eliciting wear behavior in ternary UHTCs.

Figure 6. SEM micrographs of the (**a**) 3 mm progressive scratch track and (**b**–**e**) high magnification of the selected regions eliciting wear behavior in quaternary UHTCs.

4. Conclusions

The scratch-induced wear behavior of binary, ternary and quaternary UHTCs has been evaluated under progressive loading of 1 N to 50 N with a scratch length of 3 mm. The average CoFs for binary, ternary and quaternary UHTCs are 0.43, 0.41, and 0.34, respectively. Similarly, the penetration depth and wear volume decreased from ~115.14 mm and ~6.18×10^{-3} mm^3 in binary UHTCs to ~73.48 mm and ~4.38×10^{-3} mm^3 in ternary UHTCs and ~44.41 mm and ~3.16×10^{-3} mm^3 in quaternary UHTCs. This has been attributed to the reduction in deformation under the applied load elicited from the nearly full densification, higher hardness and complete solid-solution formation in the quaternary UHTC. The scratch width at the maximum loading (50 N) decreased from 354.07 µm in the binary UHTC to 245.78 µm in the ternary UHTC and 207.12 µm in quaternary UHTC; the microstructures support this assertion. Based on the AE plot, the critical loads at which cracking, propagation and fracture initiate increased from 6.9 N, 17.6 N and 28.6 N in binary UHTCs to 10.4 N, 25.3 N and 43.6 N in ternary UHTCs and 18.5 N, 37.9 N and 48.1 N in quaternary UHTCs, respectively. Microstructural analysis of the worn-out surface elicits the dominant wear mechanisms to be pull-out, radial and edge micro-cracking, and delamination in binary and ternary UHTCs. However, grain deformation and minor delamination are the dominant wear mechanisms in quaternary UHTCs. Thus, the addition of components in UHTCs, forming a multiple-component system, has been shown to significantly improve the wear resistance of quaternary UHTCs, making them viable candidates for applications where materials undergo inelastic deformation.

References

1. Fahrenholtz, W.G.; Hilmas, G.E. Ultra-high temperature ceramics: Materials for extreme environments. *Scr. Mater.* **2017**, *129*, 94–99. [CrossRef]
2. Upadhya, K.; Yang, J.M.; Hoffman, W. Advanced materials for ultrahigh temperature structural applications above 2000 deg C. *Am. Ceram. Soc. Bull* **1997**, *76*, 23.
3. Wuchina, E.; Opila, E.; Opeka, M.; Fahrenholtz, B.; Talmy, I. UHTCs: Ultra-high temperature ceramic materials for extreme environment applications. *Electrochem. Soc. Interface* **2007**, *16*, 30. [CrossRef]
4. Zhou, Y. *Ultra-High Temperature Ceramics: Materials for Extreme Environment Applications*; American Ceramic Society/Wiley: Westerville, NJ, USA, 2014.
5. Eakins, E.; Jayaseelan, D.D.; Lee, W.E. Toward oxidation-resistant ZrB 2-SiC ultra high temperature ceramics. *Metall. Mater. Trans. A* **2011**, *42*, 878–887. [CrossRef]
6. Hwang, S.S.; Vasiliev, A.L.; Padture, N.P. Improved processing and oxidation-resistance of ZrB2 ultra-high temperature ceramics containing SiC nanodispersoids. *Mater. Sci. Eng. A* **2007**, *464*, 216–224. [CrossRef]
7. Zhang, X.-H.; Hu, P.; Han, J.-C. Structure evolution of ZrB2–SiC during the oxidation in air. *J. Mater. Res.* **2008**, *23*, 1961–1972. [CrossRef]
8. Peng, F.; Berta, Y.; Speyer, R.F. Effect of SiC, TaB2 and TaSi2 additives on the isothermal oxidation resistance of fully dense zirconium diboride. *J. Mater. Res.* **2009**, *24*, 1855–1867. [CrossRef]
9. Oses, C.; Toher, C.; Curtarolo, S. High-entropy ceramics. *Nat. Rev. Mater.* **2020**, *5*, 295–309. [CrossRef]

10. Shu, R.; Paschalidou, E.-M.; Rao, S.G.; Lu, J.; Greczynski, G.; Lewin, E.; Nyholm, L.; Le Febvrier, A.; Eklund, P. Microstructure and mechanical, electrical, and electrochemical properties of sputter-deposited multicomponent (TiNbZrTa) Nx coatings. *Surf. Coat. Technol.* **2020**, *389*, 125651. [CrossRef]

11. Nisar, A.; Zhang, C.; Boesl, B.; Agarwal, A. A perspective on challenges and opportunities in developing high entropy-ultra high temperature ceramics. *Ceram. Int.* **2020**, *46*, 25845–25853. [CrossRef]

12. Albedwawi, S.H.; AlJaberi, A.; Haidemenopoulos, G.N.; Polychronopoulou, K. High entropy oxides-exploring a paradigm of promising catalysts: A review. *Mater. Des.* **2021**, *202*, 109534. [CrossRef]

13. Feng, L.; Fahrenholtz, W.G.; Brenner, D.W. High-entropy ultra-high-temperature borides and carbides: A new class of materials for extreme environments. *Annu. Rev. Mater. Res.* **2021**, *51*, 165–185. [CrossRef]

14. Wang, F.; Monteverde, F.; Cui, B. Will high-entropy carbides and borides be enabling materials for extreme environments? *Int. J. Extrem. Manuf.* **2023**, *5*, 022002. [CrossRef]

15. Gild, J.; Zhang, Y.; Harrington, T.; Jiang, S.; Hu, T.; Quinn, M.C.; Mellor, W.M.; Zhou, N.; Vecchio, K.; Luo, J. High-entropy metal diborides: A new class of high-entropy materials and a new type of ultrahigh temperature ceramics. *Sci. Rep.* **2016**, *6*, 37946. [CrossRef]

16. Sarker, P.; Harrington, T.; Toher, C.; Oses, C.; Samiee, M.; Maria, J.-P.; Brenner, D.W.; Vecchio, K.S.; Curtarolo, S. High-entropy high-hardness metal carbides discovered by entropy descriptors. *Nat. Commun.* **2018**, *9*, 4980. [CrossRef] [PubMed]

17. Dippo, O.F.; Mesgarzadeh, N.; Harrington, T.J.; Schrader, G.D.; Vecchio, K.S. Bulk high-entropy nitrides and carbonitrides. *Sci. Rep.* **2020**, *10*, 21288. [CrossRef]

18. Moskovskikh, D.; Vorotilo, S.; Buinevich, V.; Sedegov, A.; Kuskov, K.; Khort, A.; Shuck, C.; Zhukovskyi, M.; Mukasyan, A. Extremely hard and tough high entropy nitride ceramics. *Sci. Rep.* **2020**, *10*, 19874. [CrossRef]

19. Post, B.; Glaser, F.W.; Moskowitz, D. Transition metal diborides. *Acta Metall.* **1954**, *2*, 20–25. [CrossRef]

20. Xiang, H.; Wang, J.; Zhou, Y. Theoretical predictions on intrinsic lattice thermal conductivity of ZrB3. *J. Eur. Ceram. Soc.* **2019**, *39*, 2982–2988. [CrossRef]

21. Yan, X.; Constantin, L.; Lu, Y.; Silvain, J.F.; Nastasi, M.; Cui, B. $(Hf_{0.2}Zr_{0.2}Ta_{0.2}Nb_{0.2}Ti_{0.2})$ C high-entropy ceramics with low thermal conductivity. *J. Am. Ceram. Soc.* **2018**, *101*, 4486–4491.

22. Lu, K.; Liu, J.-X.; Wei, X.-F.; Bao, W.; Wu, Y.; Li, F.; Xu, F.; Zhang, G.-J. Microstructures and mechanical properties of high-entropy $(Ti_{0.2}Zr_{0.2}Hf_{0.2}Nb_{0.2}Ta_{0.2})$ C ceramics with the addition of SiC secondary phase. *J. Eur. Ceram. Soc.* **2020**, *40*, 1839–1847. [CrossRef]

23. Han, X.; Girman, V.; Sedlak, R.; Dusza, J.; Castle, E.G.; Wang, Y.; Reece, M.; Zhang, C. Improved creep resistance of high entropy transition metal carbides. *J. Eur. Ceram. Soc.* **2020**, *40*, 2709–2715. [CrossRef]

24. Chen, H.; Xiang, H.; Dai, F.-Z.; Liu, J.; Zhou, Y. Porous high entropy $(Zr_{0.2}Hf_{0.2}Ti_{0.2}Nb_{0.2}Ta_{0.2})$ B2: A novel strategy towards making ultrahigh temperature ceramics thermal insulating. *J. Mater. Sci. Technol.* **2019**, *35*, 2404–2408.

25. Chen, H.; Xiang, H.; Dai, F.-Z.; Liu, J.; Zhou, Y. Low thermal conductivity and high porosity ZrC and HfC ceramics prepared by in-situ reduction reaction/partial sintering method for ultrahigh temperature applications. *J. Mater. Sci. Technol.* **2019**, *35*, 2778–2784. [CrossRef]

26. Sun, Q.; Tan, H.; Zhu, S.; Zhu, Z.; Wang, L.; Cheng, J.; Yang, J. Single-phase (Hf-Mo-Nb-Ta-Ti) C high-entropy ceramic: A potential high temperature anti-wear material. *Tribol. Int.* **2021**, *157*, 106883. [CrossRef]

27. Kavak, S.; Bayrak, K.G.; Bellek, M.; Mertdinç, S.; Muhaffel, F.; Gökçe, H.; Ayas, E.; Derin, B.; Öveçoğlu, M.L.; Ağaoğulları, D. Synthesis and characterization of (HfMoTiWZr) C high entropy carbide ceramics. *Ceram. Int.* **2022**, *48*, 7695–7705. [CrossRef]

28. Chen, H.; Wu, Z.; Liu, M.; Hai, W.; Sun, W. Synthesis, microstructure and mechanical properties of high-entropy (VNbTaMoW) C5 ceramics. *J. Eur. Ceram. Soc.* **2021**, *41*, 7498–7506. [CrossRef]

29. Dusza, J.; Csanádi, T.; Medveď, D.; Sedlák, R.; Vojtko, M.; Ivor, M.; Ünsal, H.; Tatarko, P.; Tatarková, M.; Šajgalík, P. Nanoindentation and tribology of a (Hf-Ta-Zr-Nb-Ti) C high-entropy carbide. *J. Eur. Ceram. Soc.* **2021**, *41*, 5417–5426. [CrossRef]

30. Jin, X.; Hou, C.; Zhao, Y.; Wang, Z.; Wang, J.; Fan, X. Mechanical properties and deformation mechanisms of $(Ti_{0.2}Zr_{0.2}Nb_{0.2}Hf_{0.2}Ta_{0.2})$C high-entropy ceramics characterized by nanoindentation and scratch tests. *Ceram. Int.* **2022**, *48*, 35445–35451. [CrossRef]

31. Nisar, A.; Balani, K. Role of Interfaces on Multi-length Scale Wear Mechanics of TaC-based Composites. *Adv. Eng. Mater.* **2017**, *19*, 1600713. [CrossRef]

32. Jaworski, R.; Pawlowski, L.; Roudet, F.; Kozerski, S.; Petit, F. Characterization of mechanical properties of suspension plasma sprayed TiO2 coatings using scratch test. *Surf. Coat. Technol.* **2008**, *202*, 2644–2653. [CrossRef]

33. Kumar, N.; Barve, S.A.; Chopade, S.S.; Kar, R.; Chand, N.; Dash, S.; Tyagi, A.K.; Patil, D.S. Scratch resistance and tribological properties of SiOx incorporated diamond-like carbon films deposited by rf plasma assisted chemical vapor deposition. *Tribol. Int.* **2015**, *84*, 124–131. [CrossRef]

34. Nisar, A.; Dolmetsch, T.; Paul, T.; Sakthivel, T.S.; Zhang, C.; Boesl, B.; Seal, S.; Agarwal, A. Unveiling enhanced oxidation resistance and mechanical integrity of multicomponent ultra-high temperature carbides. *J. Am. Ceram. Soc.* **2022**, *105*, 2500–2516. [CrossRef]

35. Nisar, A.; Sakthivel, T.; Zhang, C.; Boesl, B.; Seal, S.; Agarwal, A. Quantification of complex protective surface oxide layer formed during plasma jet exposure of multicomponent ultra-high temperature carbides. *Appl. Surf. Sci.* **2022**, *592*, 153247. [CrossRef]

36. Nisar, A.; Mohammed, M.A.K.S.; Garino, G.; Kumar, U.; John, D.; Aguiar, A.B.; Seal, S.; Agarwal, A. In-situ Crack Propagation Dynamics in Multicomponent Ultra-High Temperature Carbides. *Int. J. Refract. Met. Hard Mater.* **2024**, *125*, 106897. [CrossRef]
37. Ghosh, D.; Subhash, G.; Bourne, G.R. Room-temperature dislocation activity during mechanical deformation of polycrystalline ultra-high-temperature ceramics. *Scr. Mater.* **2009**, *61*, 1075–1078. [CrossRef]